



Measurement of isotopic separation of argon with the prototype of the cryogenic distillation plant Aria for dark matter searches

DarkSide-20k Collaboration*

Received: 25 January 2023 / Accepted: 24 March 2023
© The Author(s) 2023

Abstract The Aria cryogenic distillation plant, located in Sardinia, Italy, is a key component of the DarkSide-20k experimental program for WIMP dark matter searches at the INFN Laboratori Nazionali del Gran Sasso, Italy. Aria is designed to purify the argon, extracted from underground wells in Colorado, USA, and used as the DarkSide-20k target material, to detector-grade quality. In this paper, we report the first measurement of argon isotopic separation by distillation with the 26 m tall Aria prototype. We discuss the measurement of the operating parameters of the column and the observation of the simultaneous separation of the three stable argon isotopes: ^{36}Ar , ^{38}Ar , and ^{40}Ar . We also provide a detailed comparison of the experimental results with commercial process simulation software. This measurement of isotopic separation of argon is a significant achievement for the project, building on the success of the initial demonstration of isotopic separation of nitrogen using the same equipment in 2019.

1 Introduction

Aria is an industrial-scale plant comprising a 350 m cryogenic distillation column for isotopic separation [1], the tallest ever built, and is currently being installed in a mine shaft at Carbosulcis S.p.A., Nuraxi-Figus (SU), Italy. Aria is designed to reduce the isotopic abundance of ^{39}Ar in the low-radioactivity argon, or underground argon (UAr), extracted from underground sources and used for dark matter searches.

A full description of the Aria plant and of the column structure and performance can be found in Ref. [1]. Figure 1 shows the simplified diagram of the plant.

In recent years, interest in UAr has grown to include its use in searches for neutrino-less double-beta decay with

the LEGEND experiment [2]; in the measurement of coherent elastic neutrino-nucleus scattering with the COHERENT experiment [3]); and in measuring low-energy processes with one of the planned modules of the DUNE experiment (PNNL-SA-171088). The projected demand for UAr varies greatly, from one tonne for the COHERENT experiment to several thousand tonnes for a detector of similar size to DUNE. The required ^{39}Ar depletion factor with respect to atmospheric argon levels spans from a factor 1000 for COHERENT and DarkSide-20k to more than 10,000 for future dark matter searches with, e.g., a tonne-scale DarkSide-LowMass experiment (arXiv:2209.01177).

The first application of the Aria plant will be to purify 120 t of UAr through cryogenic distillation, which will be used in the DarkSide-20k experiment [4]. However, the high depletion factors required for future projects also demonstrate the need for isotopic separation using Aria.

The initial phase of the Aria program includes assessing the efficiency of the distillation process and determining the thermodynamic parameters of the prototype distillation plant. A successful nitrogen isotope separation campaign was conducted with the same plant in 2019 and described in Ref. [1]. The prototype plant is a shortened version of the Aria column, consisting of a top condenser, a bottom reboiler, and one central module (out of 28). It is equipped with all the auxiliary instrumentation of the full column and located in a surface building at Carbosulcis S.p.A.. The results obtained using nitrogen were very promising. However, argon has distinct thermodynamic properties, such as its boiling point in relation to pressure and its latent heat at the boiling point, compared to nitrogen. Therefore, a separate characterization of the plant's performance is necessary when using argon.

This article presents the results of a distillation run for the separation of argon isotopes conducted in 2021. Whereas ^{39}Ar is only present in traces, the two stable isotopes other than ^{40}Ar in atmospheric argon, ^{36}Ar and ^{38}Ar , have a non-negligible isotopic abundance of 0.334% and 0.063%, respectively [5,6], and can be used to characterize the distillation performance of the plant.

S. Farenzena, N. Lami, F. Lippi, N. Maccioni, C. Macia, G. M. Sabiu: not a member of the DarkSide-20k Collaboration

*e-mail: ds-ed@lngs.infn.it (corresponding author).

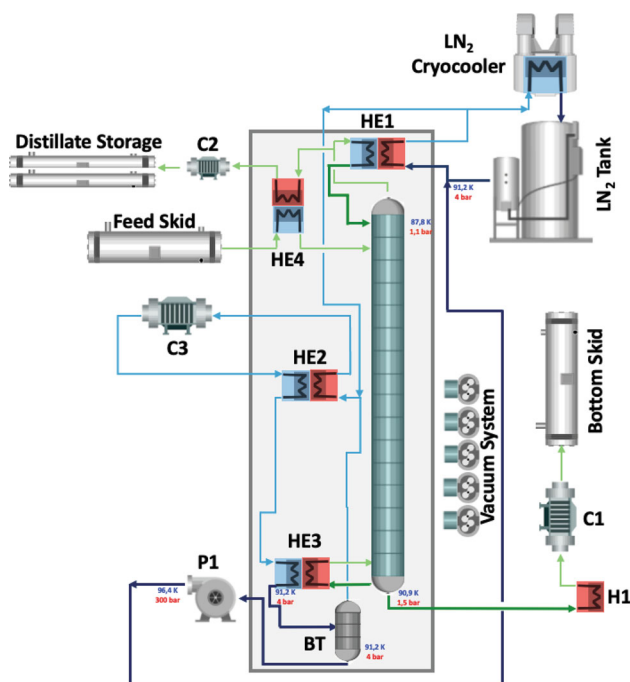


Fig. 1 Simplified diagram of the Aria plant, as reported in Ref. [1]. The column, cryogenic tanks, and heat exchangers are enclosed in a cold box (grayed area) which is vacuum-tight and designed to reduce thermal losses. The cryogenic circuit of the plant is designed with two independent loops: the argon loop (dark green lines for the liquid and light green lines for the vapor/gas) and the refrigeration loop, with nitrogen gas (cyan lines) and liquid (dark blue lines) that are used to evaporate and to condense the argon

With respect to Ref. [1], this paper presents a more in-depth characterization of the plant performance, including hydraulic parameters, details of the distillation process, and a thorough comparison between the actual performance and that obtained using a commercial process simulation software. We have also demonstrated through experimentation that multi-component distillation modeling is not required for argon distillation, despite the presence of more than two isotopes in the input feed. This was already hypothesized in Ref. [1] without experimental proof.

Here we briefly reproduce a few basic formulae of distillation columns. For a two-component distillation at total reflux, i.e. without a significant amount of argon entering or exiting the column during distillation, the separation between isotopes i and j between the top (T) and the bottom (B) of the column is given by:

$$S_{i-j}^{TB} = (\alpha_{i-j})^N, \quad (1)$$

where α_{i-j} is the relative volatility between the lighter, more volatile isotope i and the heavier, less volatile isotope j , and N is the number of theoretical stages. The separation can be measured from:

$$S_{i-j}^{TB} = \frac{(R_{i-j})_T}{(R_{i-j})_B}, \quad (2)$$

where $(R_{i-j})_{T(B)}$ is the isotopic ratio, i.e. the relative abundance between the lighter and the heavier isotope, measured at the top (bottom) of the column.

The logarithm of the relative volatility, also known as the Vapor Pressure Isotope Effect (VPIE), is given by:

$$\text{VPIE} = \ln \alpha_{i-j} \simeq \ln \frac{P_i}{P_j} \simeq \ln \frac{f_c}{f_g}, \quad (3)$$

with P_i and P_j the vapor pressures of the two isotopes i and j and f_c and f_g the reduced partition functions in the condensed phase and in the ideal gas.

In a column with structured packing like Aria, the distillation performance is related to the height equivalent to a theoretical plate or stage, HETP, and is given by:

$$\text{HETP} = \frac{h}{N} \quad (4)$$

where h is the cumulative height of the packing material of the column. Combining Eqs. (1) and (4), it follows that:

$$\text{HETP} = \frac{h \times \ln(\alpha_{i-j})}{\ln(S_{i-j}^{TB})} \quad (5)$$

The rest of the paper is organized as follows. In Sect. 2 we discuss the simulation programs used in this work. In Sect. 3 we present the experimental setup. In Sect. 4 we discuss the pressure drop along the column and the liquid holdup. In Sects. 5 and 6 we discuss the distillation measurements and in Sect. 7 we compare them with the simulations. In Sect. 8 we conclude and give some perspectives. In Appendix A we derive an estimate of the relative volatilities of ^{40}Ar with respect to ^{36}Ar and ^{38}Ar from existing measurements.

2 The simulation programs

We use the Aspen HYSYS (©2022 Aspen Technology Inc) software, a powerful tool for industrial process simulations, to model our system. HYSYS performs rigorous distillation calculations, i.e. solve the equations for mass, component, energy, and equilibrium balance for each stage of the column. Rigorous calculations also allow the simulation of multi-component distillation processes, with three or more components modeled simultaneously. The standard HYSYS library of chemicals does not include isotopes. For this simulation, we added the argon isotopes to the HYSYS library, together with their molecular weight and Antoine equation parameters.

The results for binary distillation obtained with HYSYS were compared with those from a calculation with the graphical McCabe-Thiele (MCT) method.

We also used the SulcolTM 3.5 (Sulzer) software package for structured and random packing design to model the hydraulic parameters of the distillation column. Taking input properties, such as the density and viscosity of the gas and liquid phases, the surface tension, and the mass flow rates of the gas and the liquid inside the column, Sulcol calculates column parameters including the pressure drop per unit length and the liquid hold-up of the column.

3 The experimental setup and measurements

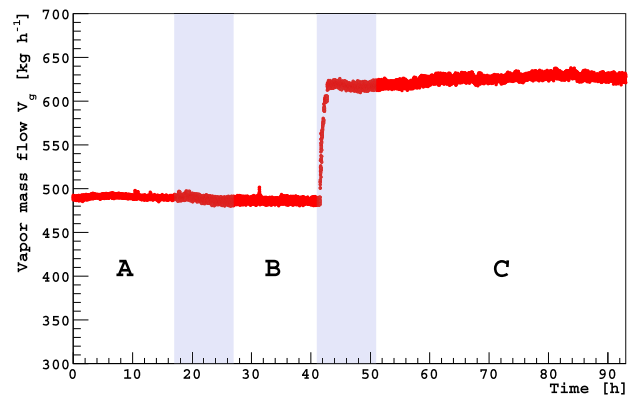
Before starting operations, the column and all the process lines were evacuated through a scroll pump. The column was then filled with argon gas. The total amount of argon filling the column was about 250 kg.

Plant operation followed a procedure similar to our previous run with nitrogen [1]. Automatic process control was implemented for most of the system. For this run, it took 12 days of operation to stabilize the plant and start the distillation measurements reported below, which lasted about 4 days. As for the past run, nitrogen was used as the refrigerant fluid.

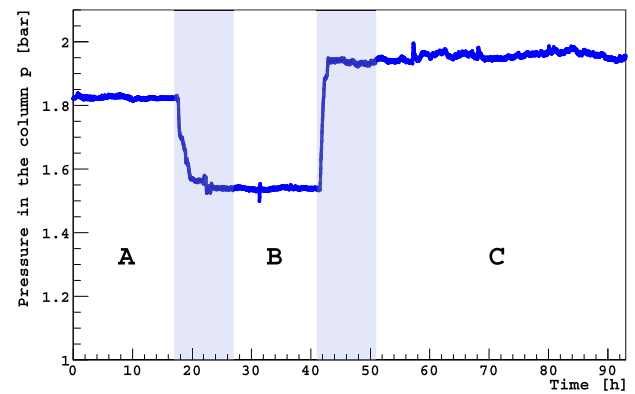
The distillation was performed in total reflux mode. About 1 L h^{-1} of gas was extracted for the sampling, corresponding to an overall loss during the run of $<0.1\%$ of the loaded argon mass. Therefore, we expect Eq. (1) to hold.

The operating conditions of the argon distillation runs are presented in Fig. 2. The top panel (Fig. 2a) displays the vapor mass flow rate of nitrogen in the auxiliary system (red); the bottom panel (Fig. 2b) shows the average pressure p inside the column (blue) as a function of time. The time averages of the same quantities are summarized in Table 1, together with the maximum pressure variation during the run, δp . The collected data is divided in three runs (A, B, and C) corresponding to changing operating conditions. At the beginning of run A, the vapor mass flow rate of nitrogen was about 10% lower than the plant design value of 550 kg h^{-1} . In run B, we kept the vapor mass flow rate unchanged and lowered the pressure inside the column by increasing the amount of nitrogen introduced into the auxiliary system. In run C we increased the vapor mass flow rate to a value about 10% higher than the design value. The lowest average pressure achieved inside the column was about 18% larger than the design value described in Ref. [1]. With argon distillation, we have achieved a ten-fold lower pressure variation during the run, than during the nitrogen distillation run discussed in Ref. [1].

Table 2 shows three derived operational parameters: the time-averaged saturation temperature, T , obtained from the Antoine equation using the measured pressures from Table 1; the argon vapor mass flow rate, V , derived from the energy balance in the reboiler; and the thermal power of the process,



(a)



(b)

Fig. 2 Vapor mass flow rate of nitrogen in the auxiliary system (red, **a**) and average pressure inside the column p (blue, **b**) as a function of time. The shaded regions correspond to periods with changing conditions in the column and are not included in the data analysis

Table 1 Time averaged operational parameters during runs A, B and C: pressure inside the column, maximum pressure variation δp during the run, and vapor mass flow rate of nitrogen in the auxiliary system

	p (bar)	δp (bar)	Vapor flow rate (kg h^{-1})
A	1.824 ± 0.001	± 0.02	491 ± 1
B	1.544 ± 0.001	± 0.02	487 ± 1
C	1.953 ± 0.001	± 0.04	624 ± 1

given by the product of nitrogen latent heat and nitrogen mass flow rate.

3.1 The gas sampling system

The instrument used to measure the isotopic distillation performance is an MKS Instruments, CirrusTM 3-XD quadrupole mass spectrometer. During the run, the mass spectrometer was continuously in operation to sample the gas coming from the top (Top) and bottom (Bottom) of the column, and from the gas bottles (Feed), as shown in Fig. 3. The gas from the

Table 2 Derived operational parameters: time-averaged saturation temperature, T , argon vapor mass flow rate, V , and the thermal power of the process, Q

	T (K)	V (kg h ⁻¹)	Q (kW)
A	93.3 ± 0.1	543 ± 1	23.0 ± 0.1
B	91.5 ± 0.1	544 ± 1	23.8 ± 0.1
C	94.0 ± 0.1	689 ± 1	29.7 ± 0.1

column flows through 1/8" copper lines between 4 m (Bottom) and 30 m (Top) in length. These lines are split before the mass spectrometer. Most of the gas flow, controlled via flow controllers set around 50 mL min⁻¹, purge the lines and is vented to air. The gas along the other branch flows through, respectively, a 1/16" (1 mm ID) stainless steel (SS), 7 cm long, capillary line; a multi-port valve (VALCO Instruments); another 1/16" (1 mm ID), 15 cm long SS capillary line; and a manual pressure regulator, to limit the gas pressure to a maximum of 1 bar, thus protecting the input of the mass spectrometer. The gas then passes through a 1/16" (1 mm ID), 1 m long SS line, and a 19 cm (0.07 mm ID) long SS capillary, to the mass spectrometer. The inlet flow of the mass spectrometer is 20 mL min⁻¹. Before the run, the response time of the sampling system was determined by connecting a bottle of argon and one of nitrogen to the multi-inlet valve. It took about 10 min to see a change in the measured gas composition and 40–45 min to see it stabilize. This lag time is caused by the combination of the relatively large buffer volume of the manual pressure regulator and the low gas inlet flow. During gas sampling of argon from the column, the inlet valve was programmed to switch among the three input capillaries every hour. This is a compromise between the response time of the sampling system and the need for quickly detect-

ing changes in isotopic mass fraction in the column when the operating parameters are changed. In Fig. 4 we show an example of a background subtracted mass spectrum from the spectrometer during the run, zoomed in the region of interest for argon isotopes and featuring well-separated peaks.

We obtain the isotopic ratios R_{36-40} and R_{38-40} as ratios of the ³⁶Ar (³⁸Ar) and ⁴⁰Ar peak heights. R_{36-40} is displayed vs time in Fig. 5, where each point corresponds to a measurement derived from a spectrum like the one in Fig. 4. Figure 5 clearly shows that the measurement of the isotopic ratio settles to a plateau in approximately 45 min. Because of this delayed response, we only considered the last 15 min of each 1-hour sampling period during the measurement of the distillation performance. The isotopic ratios were calculated with the inlet valve switched to the Bottom sampling (e.g. at times marked by dashed vertical lines). We estimated a systematic uncertainty of the order of 2% on the measured isotopic ratio due to this choice, by comparing it with other possible choices of times for calculating the isotopic ratios.

4 Pressure drop along the column and liquid holdup

The Aria column is filled with structured stainless steel packing (Sulzer CY gauze) sections 2.56 m long, four per module, interleaved with a liquid distributor to optimize flow uniformity across the column cross-section, whose structure is discussed below. The purpose of the packing is to support the liquid phase, for optimal thermodynamic contact between the rising vapor and the descending liquid. During operations, the liquid is dispersed as a film coating the surfaces of the packing and immersed in the vapor phase. This configuration is referred to as irrigated bed.

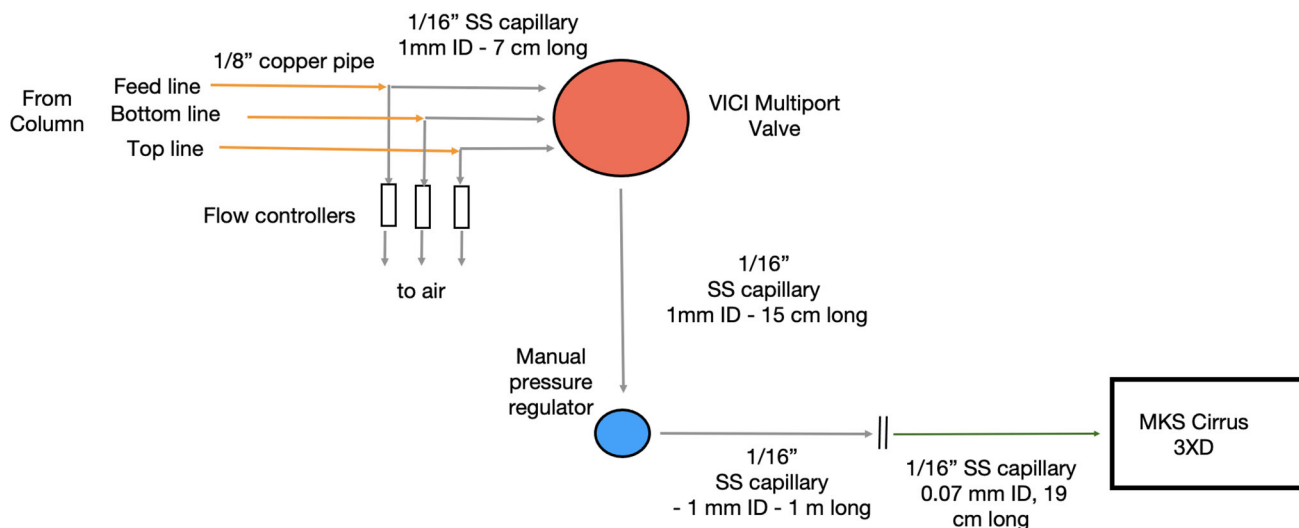


Fig. 3 Schematic of the gas sampling system

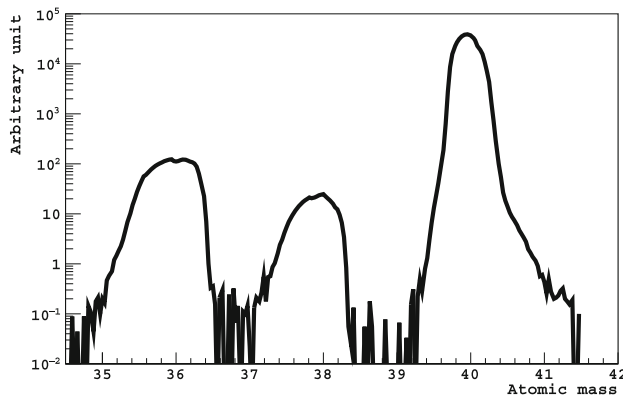


Fig. 4 Example of a background subtracted mass spectrum measured during the run, zoomed in the region of interest for argon isotopes

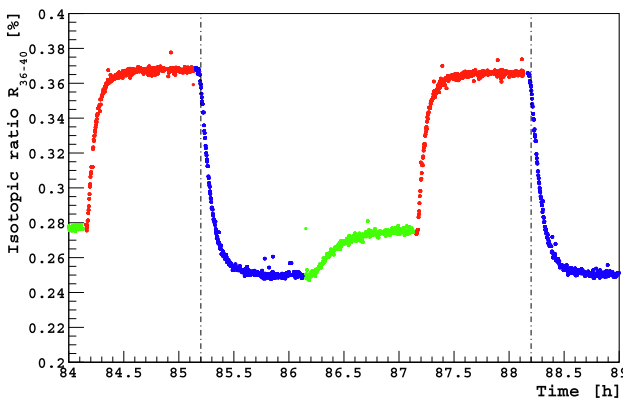


Fig. 5 Isotopic ratio, R_{36-40} , as a function of time, for a time slice of run C. Every hour, the inlet valve is switched from Top (red) to Bottom (blue) and Feed (green). The isotopic ratios were calculated at the time when the inlet valve is switched to the Bottom sampling (e.g. at times marked by dashed vertical lines), and only considering the last 15 min before each switching of the inlet valve

Two very relevant operational parameters of the packed distillation column are the pressure drop per unit length and the liquid holdup [7], described hereafter.

4.1 Pressure drop

The pressure drop is due to friction and directional changes in the gas flow inside the column caused by the packing and the distributors. Therefore, the total pressure drop in the column, Δp_{tot} , is given by the sum of the pressure drop in the distributors, $\Delta p_{distributors}$, and in the wetted packing elements, $\Delta p_{packing,irr}$ as:

$$\Delta p_{tot} = \Delta p_{distributors} + \Delta p_{packing,irr} \tag{6}$$

Table 3 Input parameters for the calculation of the concentrated loss coefficient in the distributors, ζ

Gas passage channel cross-section	a^*	0.00138 m ²
Number of gas passage channels per distributor	n_p	7
Column cross-section	A	0.079 m ²
$A^*/A = n_p \times a^*/A$		0.12

Table 4 Calculated velocity and density of the gas passing through the distributors, and pressure drop due to the distributors for runs A, B, and C from Eq. (7)

	v_G (m s ⁻¹)	ρ_G (kg m ⁻³)	$\Delta p_{distributors}$ (mbar)
A	0.202 ± 0.001	9.40 ± 0.01	1.7 ± 0.7
B	0.235 ± 0.001	8.09 ± 0.01	2.0 ± 0.9
C	0.242 ± 0.001	9.97 ± 0.01	2.6 ± 1.1

4.1.1 Calculation of the pressure drop due to the distributors

The distributors, whose picture can be found in Ref. [1], are made by horizontal plates, intercepting the downward liquid argon flow along the column. The plates are perforated, with 10 cm hollow vertical pipes or chimneys with a top cap at the hole locations on the upper side, which are uniformly distributed on the plate surface. The vapor flows up through these chimneys. The liquid formed on the distributor plate is streamed, through 0.3 cm holes located at 3 cm, 4 cm, and 5 cm height in the chimneys, to the packing section below.

In our calculations, the distributed pressure drop due to the short pipes can be neglected and the distributor is, therefore, approximated as a perforated sheet with holes. The pressure drop from the four distributors, $\Delta p_{distributors}$, is determined following Ref. [8]:

$$\Delta p_{distributors} = 4 \times \zeta \rho_G \frac{v_G^2}{2}, \tag{7}$$

where ζ is the concentrated loss coefficient, and ρ_G and v_G are the density and the velocity of the argon gas, respectively. The value of ζ is evaluated by interpolating the data reported on page 18 of Ref. [8] for ζ vs. A^*/A , and using parameters from Table 3 as input. We find $\zeta = 224 \pm 100$, with the uncertainty resulting from different parametrizations used to interpolate the data. Table 4 shows the results obtained for the three runs, with the dominant uncertainty coming from the determination of ζ .

4.1.2 Calculation of the pressure drop in the packing

The Sulcol and HYSYS programs are used to calculate the pressure drop per unit length of the packing for the dry bed, i.e. in the absence of liquid, $\Delta p_{packing,dry}/\Delta z$ (the z axis is

Table 5 Pressure drop per unit length of the packing for dry packing calculated for runs A, B, and C

$\Delta p_{\text{packing,dry}}/\Delta z$ (mbar m ⁻¹)			
	Sulcol	HYSYS	Method of Ref. [9]
A	0.45	0.49	0.38
B	0.52	0.56	0.44
C	0.68	0.73	0.55

Table 6 Pressure drop per unit length for irrigated packing calculated for runs A, B and C using the method of Ref. [9]

$\Delta p_{\text{packing,irr}}/\Delta z$ (mbar m ⁻¹)	
A	1.1 ± 0.3
B	1.2 ± 0.4
C	1.6 ± 0.4

Table 7 Total experimental, $\Delta p_{\text{tot,exp}}$, and calculated, $\Delta p_{\text{tot,calc}}$, pressure drop for tests A, B, and C

	$\Delta p_{\text{tot,exp}}$ (mbar)	$\Delta p_{\text{tot,calc}}$ (mbar)
A	16.3 ± 0.1	12.9 ± 4.0
B	14.9 ± 0.2	14.3 ± 4.5
C	19.6 ± 0.2	19.0 ± 6.0

directed downwards along the column). These calculations were cross-checked with a model for pressure drop calculation for packed columns described in Ref. [9], using the input parameters related to the packing reported in Table 14-14 of Ref. [10]. The results are summarized in Table 5 and show that the three methods agree within 30%. The pressure drop in the packing increases with the liquid load since the liquid impedes the passage of gas.

The authors of Ref. [9] also provide a method to estimate the pressure drop of the irrigated bed. Table 6 summarizes the values obtained for the pressure drop per unit length of the irrigated bed, $\Delta p_{\text{packing,irr}}/\Delta z$, which results about three times larger than that for the dry bed. We assigned an uncertainty of 30% on this number based on the comparisons of Table 5.

The total pressure drop, $\Delta p_{\text{tot,calc}}$, is given by the sum of the pressure drop of the distributors, from Table 4, and that of the irrigated packing, from Table 6 multiplied by the packing height of 10.24 m, and is shown in Table 7. Table 7 also shows the measured pressure drop of the column, $\Delta p_{\text{tot,exp}}$, i.e., the difference between the top and bottom recorded pressures (SIEMENS SITRANS P, DS III). Data and simulation show agreement within an uncertainty of the order of 30%. We will assign a corresponding uncertainty to the values of $\Delta p_{\text{packing,dry}}/\Delta z$, which will be used for comparison with Sulzer data in Fig. 8, in relation to Tables 7 and 5.

Table 8 Liquid hold-up, h_L , calculations for runs A, B, and C

h_L (%)	Sulcol	HYSYS	Our estimate
A	6.0	5.5	5.5
B	6.0	5.5	5.5
C	6.5	5.5	6.0

4.2 Liquid holdup

The liquid holdup (or retention), h_L , is the fraction of the packing volume occupied by the liquid. The holdup consists of two parts: static hold-up and dynamic hold-up. The dominant one is the dynamic hold-up, which depends on the liquid load, and, to some extent, on the gas load.

The holdup was evaluated using both HYSYS and Sulcol based on the operating conditions of the column, and with a direct calculation based on measured and estimated liquid volumes in the various elements of the plant, as described below. Given the quantity of gas initially loaded, about 250 kg, and the operating conditions of the column, we calculate that there are about 10 kg of gas and 240 kg of liquid, corresponding to 178 L. The liquid is distributed both in the packed sections and in the processing circuit. There are about 80 L at the bottom of the column, as measured by a level indicator, about 40 L in the reboiler, about 8 L in the condenser (the amount of liquid argon is related to the amount of nitrogen in the auxiliary circuit, as measured by a level indicator), about 11 L in the distributors (the height of the liquid level in the distributors during distillation must be at least 3.5 cm, which is right above the height of the first hole in the distributor pipes), and about 2 L in the piping. By subtraction, the amount of liquid in the packed sections is approximately 37 L, about 20% of the total liquid present in the column. The stainless steel structure of the packing occupies about 15% of the volume. The estimated liquid holdup is, therefore, between 5.5% and 6.0%, as shown in Table 8. This relatively low value compares well with those obtained with HYSYS and Sulcol and agrees with measurements with the same packing by others [11].

5 Measurement of distillation parameters

As is well known, to achieve correct results from mass spectrometry in the measurements of isotopic ratios, it is necessary to get calibration factors. Therefore, we applied a time-dependent correction factor to the measured isotopic ratios (R_{36-40})_T and (R_{36-40})_B, given by the ratio of the measured isotopic ratio in the feed, (R_{36-40})_F, and the known value of the natural isotopic ratio of 0.334%. Figure 6 shows the cor-

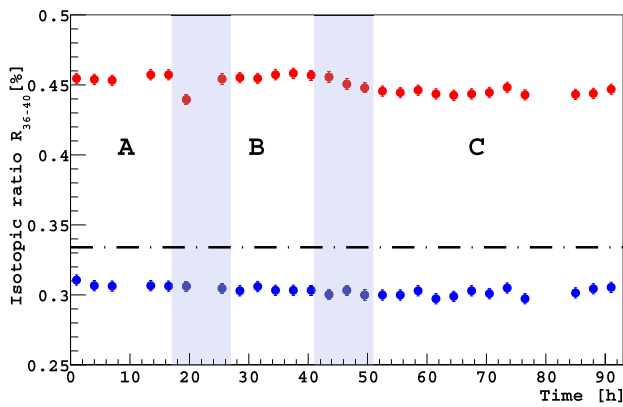


Fig. 6 The isotopic ratios $(R_{36-40})_T$ (red) and $(R_{36-40})_B$ (blue) as a function of time, after correction using the measured isotopic ratio in the feed, $(R_{36-40})_F$ (see text). The dashed-dotted line corresponds to the natural isotopic ratio. The shaded regions correspond to changing conditions in the column (see Fig. 2) and are not included in the data analysis

rected isotopic ratios $(R_{36-40})_T$ and $(R_{36-40})_B$ as a function of time. The correction also compensates for time variations in the response of the sampling system and reduces them by about a factor of ten. A systematic uncertainty on the isotopic ratios was evaluated, with reference to Fig. 4, by comparing the measurement of the isotopic ratio using the peak height value and the integral of the mass distributions. We find a $\leq 5\%$ discrepancy.

The measured separations S_{36-40}^{TB} and S_{38-40}^{TB} vs. time, defined in Eq. (2) are shown for the three runs A, B, and C in Fig. 7. Time-dependent effects in this ratio of isotopic ratios largely cancel out and lead to negligible systematic uncertainty. The comparison of the measurement of separation values with the peak height value and the integral of the mass distributions has a maximum discrepancy of about 2%, of the same size of the statistical uncertainty.

We measure one separation value every three hours, with occasional data points not available due to connectivity problems with the mass spectrometer. In runs A and B we observed a few % stability of S_{36-40}^{TB} , even though with a limited number of measurements and duration of the run. In run C $\sim 7\%$ fluctuations are observed, possibly due to small pressure variations in the column during the run. We evaluated the impact of these fluctuations on $\ln \alpha_{36-40}$ in Appendix A and found it negligible. Therefore, in the following, we use the weighted average of all measured separation values within a run.

The time-averaged separations for each run, \mathcal{S}_{36-40}^{TB} and \mathcal{S}_{38-40}^{TB} , are shown in Tables 9 and 10. The corresponding relative volatility values were determined as discussed in Appendix A, yielding an uncertainty of about 7% for $\ln \alpha_{36-40}$ and about 12% for $\ln \alpha_{38-40}$. The equivalent number of theoretical stages N and the HETP were calculated

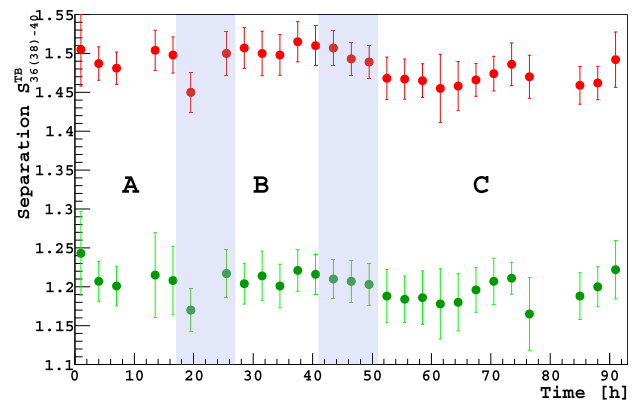


Fig. 7 Separation S_{36-40}^{TB} (red) and S_{38-40}^{TB} (green) as a function of time. The shaded regions correspond to changing conditions in the column (see Fig. 2) and are not included in the data analysis

Table 9 Time-averaged separation \mathcal{S}_{36-40}^{TB} during runs A, B, and C, logarithm of the relative volatility $\ln \alpha_{36-40}$, equivalent number of theoretical stages N and HETP

	\mathcal{S}_{36-40}^{TB}	$\ln \alpha_{36-40}$	N	HETP (cm)
A	1.49 ± 0.03	$(5.0 \pm 0.4) \times 10^{-3}$	80 ± 7	13 ± 1
B	1.51 ± 0.03	$(5.2 \pm 0.4) \times 10^{-3}$	79 ± 7	13 ± 1
C	1.48 ± 0.03	$(4.9 \pm 0.4) \times 10^{-3}$	80 ± 8	13 ± 1

Table 10 Time-averaged separation \mathcal{S}_{38-40}^{TB} during runs A, B, and C, logarithm of relative volatility $\ln \alpha_{38-40}$, equivalent number of theoretical stages N and HETP

	\mathcal{S}_{38-40}^{TB}	$\ln \alpha_{38-40}$	N	HETP (cm)
A	1.20 ± 0.04	$(2.4 \pm 0.3) \times 10^{-3}$	76 ± 17	14 ± 3
B	1.21 ± 0.03	$(2.5 \pm 0.3) \times 10^{-3}$	76 ± 13	14 ± 2
C	1.20 ± 0.03	$(2.3 \pm 0.3) \times 10^{-3}$	79 ± 15	13 ± 2

from Eqs. (1) and (5). The values of N and HETP obtained with the mass 36 and 38 isotopes and reported in the two tables agree within measurement uncertainties. Given their rather strong correlation, in the following, we only consider the measurement in Table 9.

Figure 8 shows the measured HETP (top) from Table 9 and the calculated $\Delta p_{packing,dry} / \Delta z$ (bottom) (from Table 5) vs. the sizing parameter F_G . F_G is the F-factor or vapor load and is defined as $V \times \sqrt{\rho_G}$.

The three measured values of HETP are 20–30% larger than the expectation based on the Sulzer data. This is possibly due to the different thermodynamical parameters between the argon and the fluid used by Sulzer.

The measured separations and the derived HETP are conservative estimates due to the limited data taking time (from 15 h to two days per run) at the same conditions and the somewhat larger average gas pressure in the column compared to the design value of 1.3 bar presented in Ref. [1].

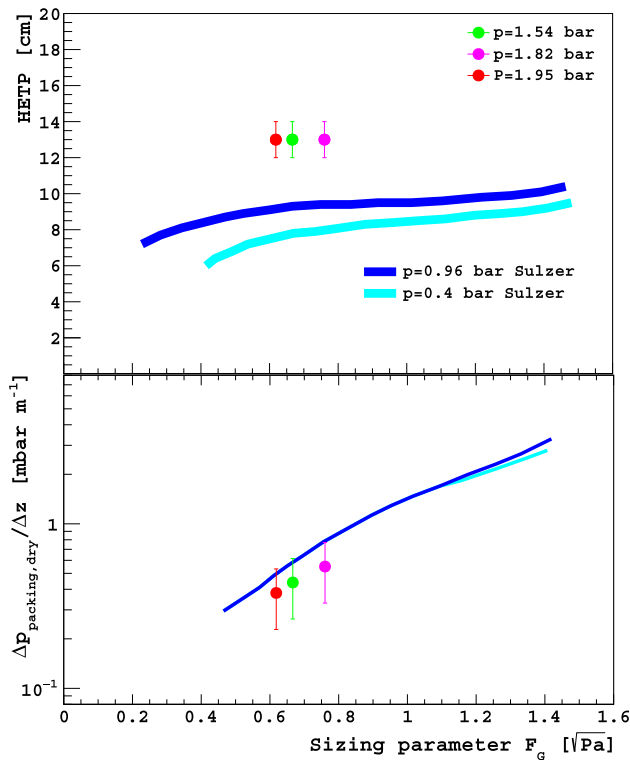


Fig. 8 Measured HETP (top), from Table 9 (red, green and violet dots), and $\Delta p_{\text{packing,dry}}/\Delta z$ (bottom), from the third column of Table 5 assuming 30% uncertainty, vs. sizing parameter, F_G , for the three runs with argon (red). Blue (cyan) line: measurements with chlorobenzene/ethylbenzene mixtures at $p_C = 0.96$ bar (0.40 bar), Sulzer CY Gauze Packing, partial data-set extracted from the Structured Packing brochure of Sulzer Ltd. A perfect match between our data and those from Sulzer is not expected due to the different thermodynamical parameters of the fluids

The measured pressure drop per unit length, which we assume for the Sulzer data to be the pressure drop per unit length for the dry bed, follows quite well the curve measured by Sulzer, within uncertainties.

6 Multi-component distillation

In the paper on nitrogen distillation [1], we argued that the distillation of ^{39}Ar would not be affected by the presence of the more abundant ^{36}Ar and ^{38}Ar , based on the argument that for a gas mixture with one dominant component and several other components with mass fractions below a few 0.1% each, the distillation of these is essentially independent of the presence of the others and is well described as a binary distillation with respect to ^{40}Ar . Therefore, a multi-component approach for distillation of argon [7] is not needed. This argument does not hold, e.g., for xenon [12]. This assumption was directly tested with this run.

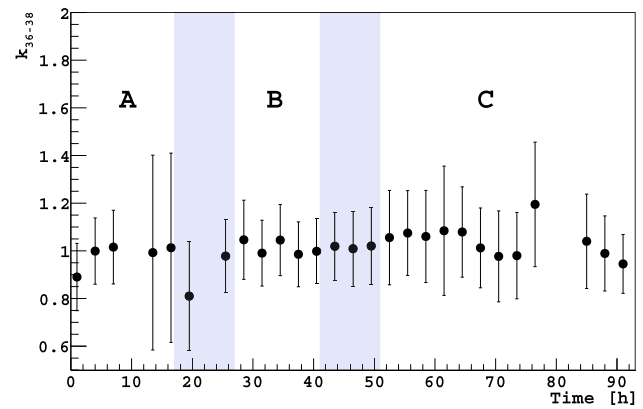


Fig. 9 Measured k_{36-38} (as defined in Eq. (10)) as a function of time. The shaded regions correspond to changing conditions in the column (see Fig. 2) and are not included in the data analysis

In total reflux condition, if the distillation ^{36}Ar and ^{38}Ar proceed independently of each other, we expect

$$S_{36-40}^{TB} = (\alpha_{36-40})^N \quad (8)$$

and

$$S_{38-40}^{TB} = (\alpha_{38-40})^N \quad (9)$$

From Eq. (A.3) one infers that:

$$k_{36-38} := \frac{\ln(S_{36-40}^{TB})}{\ln(S_{38-40}^{TB})} \times \frac{1}{2.1} = 1. \quad (10)$$

Figure 9 shows the measured value of k_{36-38} vs time. The time average of these values is 0.998 ± 0.030 , consistent with 1, and demonstrates that no multi-component approach is needed for argon distillation.

7 Comparison with simulation

The measured distillation data for run B were compared to simulations with HYSYS. We used the conditions of run B as input parameters for the simulation. These are the mean values of p from Table 1, V from Table 2, HETP from Table 9, and \mathcal{S}_{36-40}^{FB} from Table 11. The comparison of measured and simulated separations is shown in the first two columns of Table 11. Good agreement is observed within the uncertainties. The simulation was also performed for binary systems using both the rigorous and the MCT methods. The latter is included for completeness and because of its use in Ref. [1]. We find good agreement across the board.

8 Conclusions and outlook

We validated the performance of the Aria plant with argon running the prototype plant for a few days in total reflux. We

Table 11 Comparison of separations between measurements and simulation, related to run B conditions: data (Exp.) from Tables 9 and 10, HYSYS rigorous simulation with three components (Rig. 3), with two components (Rig. 2) and McCabe-Thiele (MCT) simulation

	Exp.	Rig. 3	Rig. 2	MCT
\mathcal{S}_{36-40}^{TB}	1.51 ± 0.03	1.5 ± 0.1	1.5 ± 0.1	1.5 ± 0.1
\mathcal{S}_{38-40}^{TB}	1.21 ± 0.03	1.20 ± 0.04		

significantly improved our understanding of the plant performance compared to the previous nitrogen distillation run, achieving a deeper understanding of operating characteristics such as the hydraulic parameters and the behavior of multi-component distillation. We also successfully modeled the Aria prototype performance using commercial process simulation software. This study is a validation of both the plant behavior and the software itself. Originally designed for distilling organic compounds at room temperature, it is also suitable for the simulation of cryogenic isotopic distillation.

The average measured HETP is about 30% larger than that measured in a different column with the same packing, using organic mixtures at room temperature by Sulzer. The discrepancy could be due to the different thermodynamical parameters of the fluids used in the two cases or to the somewhat larger average gas pressure in the column compared to the design value of 1.3 bar presented in Ref. [1]. If the HETP values reported in this article were the real ones, the Aria performance forecasts reported in Table 3 of Ref. [1] would be modified so that, with the same separation factor between ^{39}Ar and ^{40}Ar of 19, the mass flow rate in the bottom stream, B, would decrease from 6.73 to $3.94 \pm 0.30 \text{ kg day}^{-1}$.

The measured pressure drop per unit length is in agreement, within uncertainties, with that measured with the organic mixture.

Acknowledgements This report is based upon work supported by FSC 2014-2020 - Patto per lo Sviluppo, Regione Sardegna, Italy, the U. S. National Science Foundation (NSF) (Grants No. PHY-0919363, No. PHY-1004054, No. PHY-1004072, No. PHY-1242585, No. PHY-1314483, No. PHY-1314507, associated collaborative grants, No. PHY-1211308, No. PHY-1314501, and No. PHY-1455351, as well as Major Research Instrumentation Grant No. MRI-1429544), the Italian Istituto Nazionale di Fisica Nucleare (Grants from Italian Ministero dell'Istruzione, Università, e Ricerca Progetto Premiale 2013 and Commissione Scientific Nazionale II), the Natural Sciences and Engineering Research Council of Canada, SNOLAB, and the Arthur B. McDonald Canadian Astroparticle Physics Research Institute. We acknowledge the financial support by LabEx UnivEarthS (ANR-10-LABX-0023 and ANR18-IDEX-0001), the São Paulo Research Foundation (Grant FAPESP-2017/26238-4), Chinese Academy of Sciences (113111KY5B20210030) and National Natural Science Foundation of China (12020101004). The authors were also supported by the Spanish Ministry of Science and Innovation (MICINN) through the grant PID2019-109374GB-I00, the "Atracción de Talento" Grant 2018-T2/TIC-10494, the Polish NCN, Grant No. UMO-2019/33/B/ST2/

02884, the Polish Ministry of Science and Higher Education, MNI-SW, grant number 6811/IA/SP/2018, the International Research Agenda Programme AstroCeNT, Grant No. MAB/2018/7, funded by the Foundation for Polish Science from the European Regional Development Fund, the European Union's Horizon 2020 research and innovation program under grant agreement No 952480 (DarkWave), the Science and Technology Facilities Council, part of the United Kingdom Research and Innovation, and The Royal Society (United Kingdom), and IN2P3-COPIN consortium (Grant No. 20-152). I.F.M.A is supported in part by Conselho Nacional de Desenvolvimento Científico e Tecnológico (CNPq). We also wish to acknowledge the support from Pacific Northwest National Laboratory, which is operated by Battelle for the U.S. Department of Energy under Contract No. DE-AC05-76RL01830. This research was supported by the Fermi National Accelerator Laboratory (Fermilab), a U.S. Department of Energy, Office of Science, HEP User Facility. Fermilab is managed by Fermi Research Alliance, LLC (FRA), acting under Contract No. DE-AC02-07CH11359. We acknowledge the professional contribution of the Mine and Electrical Maintenance staff of Carbosulcis S.p.A. to this activity. We thank Polaris S.r.L. and in particular M. Masetto and E.V.Canesi for their continuous support during the preparation and execution of the run. We thank Fondazione Aria for its contribution to the project and, in particular, for the help during the data-taking. We thank S.Nisi of Istituto Nazionale di Fisica Nucleare, Laboratori Nazionali del Gran Sasso, for his contribution in the commissioning of the sampling system and M.Guetti of Istituto Nazionale di Fisica Nucleare, Laboratori Nazionali del Gran Sasso, for the help in plant maintenance. We thank M. Arba and M. Tuveri of the Cagliari Division of Istituto Nazionale di Fisica Nucleare for their support during the preparation of the run. We acknowledge the contribution of eng. S. Tosti, T. Pinna, D.Dongiovanni, A.Santucci of ENEA for the safety analyses for Aria.

Data Availability Statement This manuscript has no associated data or the data will not be deposited. [Authors' comment: The datasets generated during and/or analysed during the current study are available from the corresponding author on reasonable request.]

Open Access This article is licensed under a Creative Commons Attribution 4.0 International License, which permits use, sharing, adaptation, distribution and reproduction in any medium or format, as long as you give appropriate credit to the original author(s) and the source, provide a link to the Creative Commons licence, and indicate if changes were made. The images or other third party material in this article are included in the article's Creative Commons licence, unless indicated otherwise in a credit line to the material. If material is not included in the article's Creative Commons licence and your intended use is not permitted by statutory regulation or exceeds the permitted use, you will need to obtain permission directly from the copyright holder. To view a copy of this licence, visit <http://creativecommons.org/licenses/by/4.0/>.

Funded by SCOAP³. SCOAP³ supports the goals of the International Year of Basic Sciences for Sustainable Development.

Appendix A: Evaluation of relative volatilities

In this section, we give an update of our best estimate of the relative volatilities α_{36-40} and α_{38-40} , based on the scrutiny of the literature, and we update the result derived in Appendix A of Ref. [1]. For $\ln \alpha_{36-40}$, we included measurements from Ref. [13] and from Ref. [14], corresponding to the second definition of relative volatility of Eq. (3).

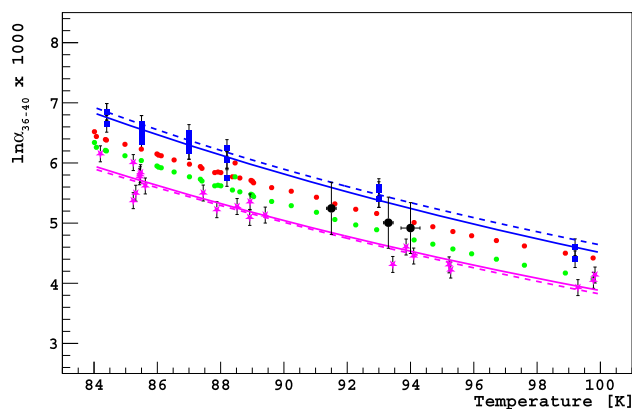


Fig. 10 Measurements of $\ln \alpha_{36-40}$ vs. temperature. The data are taken from [15] (blue squares), [13] (violet stars), and [14] (green and red dots). The function $\ln \alpha_{36-40} = A \times 1/T^2 + B$ is fitted (continuous lines) to the data of Ref. [15] and Ref. [13]. The corresponding one-sided standard deviation curves (dashed lines) are also shown. The derived values of $\ln \alpha_{36-40}$ corresponding to the three runs A, B, and C are also shown (black dots)

In Fig. 10 we report the measured dependence of $\ln \alpha_{36-40}$ on temperature. The function $\ln \alpha_{36-40} = A \times 1/T^2 + B$ is fitted to the data of Ref. [15] and Ref. [13]. The choice of this parametrization follows the theoretical considerations of Ref. [16]. The errors on the single measurement were set all equal in the fit and determined in retrospect requiring the reduced χ^2 to be one. Applying error propagation for the estimate of $\ln \hat{\alpha}_{36-40} = \hat{A} \times 1/T^2 + \hat{B}$ and of the uncertainty $\sigma_{\ln \hat{\alpha}}$ as:

$$\sigma_{\ln \hat{\alpha}} = \sqrt{V_{00} \times (1/T^2)^2 + V_{11} + 2/T^2 \times V_{22}} \quad (\text{A.1})$$

with V_{ij} being the elements of the covariance matrix, one obtains the mean (continuous lines) and one-sided standard deviation curves (dashed lines). To take into account all existing measurements in our estimate, we assumed that the one standard deviation value of $\ln \alpha_{36-40}$ at a given temperature lies inside the two dashed curves. The values of $\ln \alpha_{36-40}$ corresponding to the temperatures of the three runs A, B, and C are also shown and their values are reported in Table 9. The horizontal error bars correspond to the uncertainty on the temperature related to the pressure variations during the runs of Table 1. They give a negligible contribution to the uncertainty on $\ln \alpha_{36-40}$.

The relative volatility $\ln \alpha_{38-40}$, at given temperature, was derived from $\ln \alpha_{36-40}$ using the theoretical formula from Ref. [17], Eq. (25):

$$\ln \alpha_{A-40} \propto \frac{40 - A}{A^3}, \quad (\text{A.2})$$

with A the atomic mass of an isotope, which entails:

$$\ln \alpha_{36-40} \sim \ln \alpha_{38-40} \times 2.1. \quad (\text{A.3})$$

This dependence is also consistent, within errors, with the measurements of Ref. [18], of $\ln \alpha_{36-40} = \ln \alpha_{38-40} \times (2.3 \pm 0.2)$ at 87.3 K. The relative uncertainty from these measurements was propagated on the final estimate of the quantity $\ln \alpha_{38-40}$.

References

1. P. Agnes, S. Albergo, I. F. M. Albuquerque, T. Alexander, A. Alici, A. K. Alton, P. Amaudruz, M. Arba, P. Arpaia, S. Arcelli, et al. (DarkSide-20k Collaboration). *Eur. Phys. J. C* **81**(4), 359 (2021)
2. N. Abgrall, A. Abramov, N. Abrosimov, I. Abt, M. Agostini, M. Agartioglu, A. Ajaq, S.I. Alvis, F.T. Avignone III., X. Bai et al., *AIP Conf. Proc.* **1894**, 020027 (2017)
3. D. Akimov, P. An, C. Awe, P.S. Barbeau, B. Becker, V. Belov, M.A. Blackston, A. Bolozdynya, B. Cabrera-Palmer, N. Chen et al., *Phys. Rev. Lett.* **126**, 012002 (2021)
4. C.E. Aalseth, F. Acerbi, P. Agnes, I.F.M. Albuquerque, T. Alexander, A. Alici, A.K. Alton, P. Antonioli, S. Arcelli, R. Ardito et al., DarkSide-20k Collaboration. *Eur. Phys. J. Plus* **133**, 131 (2018)
5. J.-Y. Lee, K. Marti, J.P. Severinghaus, K. Kawamura, H.-S. Yoo, J. Bok Lee, J. Seog Kim, *Geochim. Cosmochim. Acta* **70**, 4507 (2006)
6. J.K. Böhlke, *Pure Appl. Chem.* **86**, 1421 (2014)
7. H.Z. Kister, J.R. Haas, D.R. Hart, D.R. Gill, *Distillation Design* (McGraw-Hill, New York, 1992)
8. M. Doninelli, M. Doninelli, *Idraulica* **28**, 3 (2005)
9. J. Stilmair, J.L. Bravo, J.R. Fair, *Gas Sep. Purif.* **3**, 19 (1989)
10. D.W. Green, M.Z. Southard, *Perry's chemical engineer's handbook*, 9th edn. (McGraw-Hill, New York, 2019)
11. J. Lévêque, D. Rouzineau, M. Prévost, M. Meyer, *Chem. Eng. Sci.* **64**, 2607 (2009)
12. H.O. Back, D.R. Bottenus, C. Clayton, D. Stephenson, W. TeGrotenhuis, *J. Instrum.* **12**, 09033 (2017)
13. J.T. Phillips, C.U. Linderstrom-Lang, J. Bigeleisen, *J. Chem. Phys.* **56**, 5053 (1972)
14. M.W. Lee, S. Fuks, J. Bigeleisen, *J. Chem. Phys.* **53**, 4066 (1970)
15. G. Boato, G. Casanova, G. Scoles, M.E. Vallauri, *Nuovo Cim.* **20**, 88 (1961)
16. G. Boato, G. Casanova, A. Levi, *J. Chem. Phys.* **37**, 201 (1962)
17. J.N. Canongia Lopes, A.A.H. Pádua, L.P.N. Rebelo, J. Bigeleisen, *J. Chem. Phys.* **118**, 5028 (2003)
18. A. Alamre, I. Badhress, B. Death, C. Licciardi, D. Sinclair, *ACS Omega* **5**, 28977 (2020)

DarkSide-20k Collaboration*

E. Aaron⁴⁹, P. Agnes³⁰, I. Ahmad⁶⁶, S. Albergo^{2,3}, I. F. M. Albuquerque⁴, T. Alexander⁵, A. K. Alton⁸, P. Amaudruz⁹, M. Atzori Corona^{21,28}, M. Ave⁴, I. Ch. Avetisov¹⁰, O. Azzolini¹¹, H. O. Back⁵, Z. Balmforth¹², A. Barrado Olmedo¹⁴, P. Barrillon¹⁵, A. Basco¹⁶, G. Batignani^{17,18}, V. Bocci⁴¹, W. M. Bonivento²¹, B. Bottino^{22,23}, M. G. Boulay²⁴, J. Busto¹⁵, M. Cadeddu²¹, A. Caminata²³, N. Canci¹⁶, A. Capra⁹, S. Caprioli²³, M. Caravati²¹, N. Cargioli^{21,28}, M. Carlini²⁹, P. Castello^{21,32}, P. Cavalcante²⁹, S. Cavuoti^{16,33,35}, S. Cebrian³⁶, J. M. Cela Ruiz¹⁴, S. Chashin¹³, A. Chepurinov¹³, E. Chyhyrnyets¹¹, L. Cifarelli^{6,7}, D. Cintas³⁶, M. Citterio³⁸, B. Cleveland^{68,69}, V. Cocco²¹, E. Conde Vilda¹⁴, L. Consiglio²⁹, S. Copello^{22,23}, G. Covone^{16,33}, M. Czubak³⁷, M. D’Aniello³⁴, S. D’Auria³⁸, M. D. Da Rocha Rolo³⁹, S. Davini²³, S. De Cecco^{41,42}, G. De Guido⁴⁵, D. De Gruttola^{43,44}, S. De Pasquale^{43,44}, G. De Rosa^{16,33}, G. Dellacasa³⁹, A. V. Derbin⁴⁶, A. Devoto^{21,28}, F. Di Capua^{16,33}, L. Di Noto²³, P. Di Stefano⁷³, G. Dolganov⁴⁷, F. Dordei²¹, E. Ellingwood⁷³, T. Erjavec⁴⁹, S. Farenzena⁹⁵, M. Fernandez Diaz¹⁴, G. Fiorillo^{16,33}, P. Franchini^{12,74}, D. Franco⁵¹, N. Funicello^{43,44}, F. Gabriele²¹, D. Gahan^{21,28}, C. Galbiati^{29,30,52}, G. Gallina⁵², G. Gallus^{21,32}, M. Garbini^{7,31}, P. Garcia Abia¹⁴, A. Gendotti⁵³, C. Ghiano²⁹, C. Giganti⁴⁰, G. K. Giovanetti⁵⁵, V. Goicoechea Casanueva⁵⁶, A. Gola^{57,58}, G. Grauso¹⁶, G. Grilli di Cortona⁵⁰, A. Grobov^{47,60}, M. Gromov^{13,61}, M. Guan⁶², M. Guerzoni⁷, M. Gulino^{63,64}, C. Guo⁶², B. R. Hackett⁵, A. L. Hallin⁶⁵, A. Hamer^{12,92}, M. Haranczyk³⁷, T. Hessel⁵¹, S. Hill¹², S. Horikawa^{29,94}, F. Hubaut¹⁵, J. Hucker⁷³, T. Hugues^{51,66}, An. Ianni^{29,52}, V. Ippolito⁴¹, C. Jillings^{68,69}, S. Jois¹², P. Kachru^{29,30}, A. A. Kemp⁷³, C. L. Kendziora⁶⁷, M. Kimura⁶⁶, I. Kochanek²⁹, K. Kondo²⁹, G. Korga¹², S. Koulosousas¹², A. Kubankin⁷⁰, M. Kuss¹⁷, M. Kuźniak⁶⁶, M. La Commara^{16,71}, M. Lai^{21,28}, N. Lami⁹⁵, E. Le Guirriec¹⁵, E. Leason¹², A. Leoni²⁹, L. Lidey⁵, F. Lippi⁹⁵, M. Lissia²¹, L. Luzzi¹⁴, O. Lychagina⁶¹, N. Maccioni⁹⁵, O. Macfadyen¹², I. N. Machulin^{47,60}, S. Manecki^{68,69}, I. Manthos⁸⁹, L. Mapelli⁵², A. Margotti⁷, S. M. Mari^{26,27}, C. Mariani⁸⁰, J. Maricic⁵⁶, A. Marini^{22,23}, M. Martínez^{36,72}, C. J. Martoff⁹¹, M. Mascia⁸⁴, A. Masoni²¹, G. Matteucci^{16,33}, K. Mavrokoridis⁸⁸, C. Maxia⁹⁵, A. B. McDonald⁷³, A. Messina^{41,42}, R. Milincic⁵⁶, A. Mitra⁹³, A. Moharana^{29,30}, S. Moiola⁴⁵, J. Monroe¹², E. Moretti⁵⁷, M. Morrocchi^{17,18}, T. Mróz³⁷, V. N. Muratova⁴⁶, C. Muscas^{21,32}, P. Musico²³, R. Nania⁷, M. Nessi²⁹, K. Nikolopoulos⁸⁹, J. Nowak⁹, K. Olchansky⁹, A. Oleinik⁷⁰, V. Oleynikov^{19,20}, P. Organtini^{29,52}, A. Ortiz de Solórzano³⁶, L. Pagani⁴⁹, M. Pallavicini^{22,23}, L. Pandola⁶⁴, E. Pantic⁴⁹, E. Paoloni^{17,18}, G. Paternoster^{57,58}, P. A. Pegoraro^{21,32}, K. Pelczar³⁷, L. A. Pellegrini⁴⁵, C. Pellegrino⁷, V. Pseudo¹⁴, S. Piacentini^{41,42}, L. Pietrofaccia²⁹, N. Pino^{2,3}, A. Pocar⁴⁸, D. M. Poehlmann⁴⁹, S. Pordes⁶⁷, P. Pralavorio¹⁵, D. Price⁷⁶, F. Ragusa^{38,77}, Y. Ramachers⁹³, M. Razeti²¹, A. L. Renshaw¹, M. Rescigno⁴¹, F. Retiere⁹, L. P. Rignanese^{7,6}, C. Ripoli^{43,44}, A. Rivetti³⁹, A. Roberts⁸⁸, C. Roberts⁸⁸, J. Rode^{40,51}, G. Rogers⁸⁹, L. Romero¹⁴, M. Rossi^{22,23}, A. Rubbia⁵³, M. A. Sabia^{41,42}, G. M. Sabiu⁹⁵, P. Salomone^{41,42}, E. Sandford⁷⁶, S. Sanfilippo⁶⁴, D. Santone¹², R. Santorelli¹⁴, C. Savarese⁵², E. Scapparone⁷, G. Schillaci⁶⁴, F. Schukman⁷³, G. Scioli^{6,7}, M. Simeone^{16,79}, P. Skensved⁷³, M. D. Skorokhvatov^{47,60}, O. Smirnov⁶¹, T. Smirnova⁴⁷, B. Smith⁹, F. Spadoni⁵, M. Spangenberg⁹³, R. Stefanizzi^{21,28}, A. Steri²¹, V. Stornelli^{29,94}, S. Stracka¹⁷, M. Stringer⁷³, S. Sulis^{21,32}, A. Sung⁵², Y. Suvorov^{16,33,47}, A. M. Szalc⁹², R. Tartaglia²⁹, A. Taylor⁸⁸, J. Taylor⁸⁸, S. Tedesco^{39,54}, G. Testera²³, K. Thieme⁵⁶, T. N. Thorpe⁸¹, A. Tonazzo⁵¹, A. Tricomi^{2,3}, E. V. Unzhakov⁴⁶, T. Vallivilayil John^{29,30}, M. Van Uffelen¹⁵, T. Viant⁵³, S. Viel²⁴, R. B. Vogelaar⁸⁰, J. Vosseveld⁸⁸, M. Wada^{28,66}, M. B. Walczak⁶⁶, H. Wang⁸¹, Y. Wang^{62,85}, S. Westerdale^{52,87}, L. Williams⁸², I. Wingerter-Seez¹⁵, R. Wojaczyński⁶⁶, Ma. M. Wojcik³⁷, T. Wright⁸⁰, Y. Xie^{62,85}, C. Yang^{62,85}, A. Zabihi⁶⁶, P. Zakhary⁶⁶, A. Zani³⁸, A. Zichichi^{6,7}, G. Zuzel³⁷, M. P. Zykova¹⁰

¹ Department of Physics, University of Houston, Houston, TX 77204, USA² INFN Catania, Catania 95121, Italy³ Università of Catania, Catania 95124, Italy⁴ Instituto de Física, Universidade de São Paulo, São Paulo 05508-090, Brazil⁵ Pacific Northwest National Laboratory, Richland, WA 99352, USA⁶ Department of Physics and Astronomy, Università degli Studi di Bologna, 40126 Bologna, Italy⁷ INFN Bologna, 40126 Bologna, Italy⁸ Physics Department, Augustana University, Sioux Falls, SD 57197, USA⁹ TRIUMF, 4004 Wesbrook Mall, Vancouver, BC V6T 2A3, Canada¹⁰ Mendeleev University of Chemical Technology, Moscow 125047, Russia¹¹ INFN Laboratori Nazionali di Legnaro, 35020 Legnaro, Padova, Italy¹² Department of Physics, Royal Holloway University of London, Egham TW20 0EX, UK¹³ Skobeltsyn Institute of Nuclear Physics, Lomonosov Moscow State University, Moscow 119234, Russia¹⁴ CIEMAT, Centro de Investigaciones Energéticas, Medioambientales y Tecnológicas, Madrid 28040, Spain

- 15 Centre de Physique des Particules de Marseille, Aix Marseille Univ, CNRS/IN2P3, CPPM, Marseille, France
- 16 INFN Napoli, 80126 Naples, Italy
- 17 INFN Pisa, 56127 Pisa, Italy
- 18 Physics Department, Università degli Studi di Pisa, 56127 Pisa, Italy
- 19 Budker Institute of Nuclear Physics, Novosibirsk 630090, Russia
- 20 Novosibirsk State University, Novosibirsk 630090, Russia
- 21 INFN Cagliari, 09042 Cagliari, Italy
- 22 Physics Department, Università degli Studi di Genova, 16146 Genova, Italy
- 23 INFN Genova, 16146 Genova, Italy
- 24 Department of Physics, Carleton University, Ottawa, ON K1S 5B6, Canada
- 25 CERN, European Organization for Nuclear Research, 1211 Geneva 23, Switzerland
- 26 INFN Roma Tre, 00146 Rome, Italy
- 27 Mathematics and Physics Department, Università degli Studi Roma Tre, 00146 Rome, Italy
- 28 Physics Department, Università degli Studi di Cagliari, 09042 Cagliari, Italy
- 29 INFN Laboratori Nazionali del Gran Sasso, 67100 Assergi, AQ, Italy
- 30 Gran Sasso Science Institute, 67100 L'Aquila, Italy
- 31 Museo Storico della Fisica e Centro Studi e Ricerche Enrico Fermi, 00184 Rome, Italy
- 32 Department of Electrical and Electronic Engineering, Università degli Studi di Cagliari, 09123 Cagliari, Italy
- 33 Physics Department, Università degli Studi "Federico II" di Napoli, 80126 Naples, Italy
- 34 Department of Strutture per l'Ingegneria e l'Architettura, Università degli Studi "Federico II" di Napoli, 80131 Naples, Italy
- 35 INAF Osservatorio Astronomico di Capodimonte, 80131 Naples, Italy
- 36 Centro de Astropartículas y Física de Altas Energías, Universidad de Zaragoza, 50009 Zaragoza, Spain
- 37 M. Smoluchowski Institute of Physics, Jagiellonian University, 30-348 Krakow, Poland
- 38 INFN Milano, 20133 Milan, Italy
- 39 INFN Torino, 10125 Turin, Italy
- 40 LPNHE, CNRS/IN2P3, Sorbonne Université, Université Paris Diderot, Paris 75252, France
- 41 INFN Sezione di Roma, 00185 Rome, Italy
- 42 Physics Department, Sapienza Università di Roma, 00185 Rome, Italy
- 43 Physics Department, Università degli Studi di Salerno, 84084 Salerno, Italy
- 44 INFN Gruppo Collegato di Salerno, Sezione di Napoli, 84084 Salerno, Italy
- 45 Chemistry, Materials and Chemical Engineering Department "G. Natta", Politecnico di Milano, 20133 Milan, Italy
- 46 Saint Petersburg Nuclear Physics Institute, Gatchina 188350, Russia
- 47 National Research Centre Kurchatov Institute, Moscow 123182, Russia
- 48 Amherst Center for Fundamental Interactions and Physics Department, University of Massachusetts, Amherst, MA 01003, USA
- 49 Department of Physics, University of California, Davis, CA 95616, USA
- 50 INFN Laboratori Nazionali di Frascati, 00044 Frascati, Italy
- 51 APC, Université de Paris, CNRS, Astroparticule et Cosmologie, 75013 Paris, France
- 52 Physics Department, Princeton University, Princeton, NJ 08544, USA
- 53 Institute for Particle Physics, ETH Zürich, Zürich 8093, Switzerland
- 54 Department of Electronics and Communications, Politecnico di Torino, 10129 Turin, Italy
- 55 Williams College, Physics Department, Williamstown, MA 01267, USA
- 56 Department of Physics and Astronomy, University of Hawai'i, Honolulu, HI 96822, USA
- 57 Fondazione Bruno Kessler, Povo 38123, Italy
- 58 Trento Institute for Fundamental Physics and Applications, 38123 Povo, Italy
- 59 Universitat de Barcelona, Barcelona E-08028, Catalonia, Spain
- 60 National Research Nuclear University MEPhI, Moscow 115409, Russia
- 61 Joint Institute for Nuclear Research, Dubna 141980, Russia
- 62 Institute of High Energy Physics, Beijing 100049, China
- 63 Engineering and Architecture Faculty, Università di Enna Kore, 94100 Enna, Italy
- 64 INFN Laboratori Nazionali del Sud, 95123 Catania, Italy
- 65 Department of Physics, University of Alberta, Edmonton, AB T6G 2R3, Canada

- ⁶⁶ AstroCeNT, Nicolaus Copernicus Astronomical Center of the Polish Academy of Sciences, 00-614 Warsaw, Poland
- ⁶⁷ Fermi National Accelerator Laboratory, Batavia, IL 60510, USA
- ⁶⁸ SNOLAB, Lively, ON P3Y 1N2, Canada
- ⁶⁹ Department of Physics and Astronomy, Laurentian University, Sudbury, ON P3E 2C6, Canada
- ⁷⁰ Radiation Physics Laboratory, Belgorod National Research University, Belgorod 308007, Russia
- ⁷¹ Pharmacy Department, Università degli Studi “Federico II” di Napoli, 80131 Naples, Italy
- ⁷² Fundación ARAID, Universidad de Zaragoza, Zaragoza 50009, Spain
- ⁷³ Department of Physics, Engineering Physics and Astronomy, Queen’s University, Kingston, ON K7L 3N6, Canada
- ⁷⁴ Physics Department, Lancaster University, Lancaster LA1 4YB, UK
- ⁷⁵ Civil and Environmental Engineering Department, Politecnico di Milano, 20133 Milan, Italy
- ⁷⁶ Department of Physics and Astronomy, The University of Manchester, Manchester M13 9PL, UK
- ⁷⁷ Physics Department, Università degli Studi di Milano, 20133 Milan, Italy
- ⁷⁸ Brookhaven National Laboratory, Upton, NY 11973, USA
- ⁷⁹ Chemical, Materials, and Industrial Production Engineering Department, Università degli Studi “Federico II” di Napoli, Napoli 80126, Italy
- ⁸⁰ Virginia Tech, Blacksburg, VA 24061, USA
- ⁸¹ Physics and Astronomy Department, University of California, Los Angeles, CA 90095, USA
- ⁸² Department of Physics and Engineering, Fort Lewis College, Durango, CO 81301, USA
- ⁸³ Institute of Applied Radiation Chemistry, Lodz University of Technology, 93-590 Lodz, Poland
- ⁸⁴ Department of Mechanical, Chemical, and Materials Engineering, Università degli Studi, 09042 Cagliari, Italy
- ⁸⁵ University of Chinese Academy of Sciences, Beijing 100049, China
- ⁸⁶ Institut für Kernphysik, Johannes Gutenberg-Universität Mainz, 55128 Mainz, Germany
- ⁸⁷ Department of Physics and Astronomy, University of California, Riverside, CA 92507, USA
- ⁸⁸ Department of Physics, University of Liverpool, The Oliver Lodge Laboratory, Liverpool L69 7ZE, UK
- ⁸⁹ School of Physics and Astronomy, University of Birmingham, Edgbaston, B15 2TT Birmingham, UK
- ⁹⁰ Science and Technology Facilities Council (STFC), Rutherford Appleton Laboratory, Technology, Harwell Oxford, Didcot OX11 0QX, UK
- ⁹¹ Physics Department, Temple University, Philadelphia, PA 19122, USA
- ⁹² School of Physics and Astronomy, University of Edinburgh, Edinburgh EH9 3FD, UK
- ⁹³ Department of Physics, University of Warwick, Coventry CV47AL, UK
- ⁹⁴ Università degli Studi dell’Aquila, 67100 L’Aquila, Italy
- ⁹⁵ CarboSulcis S.p.A.-Miniera Monte Sinni, 09010 Gonnese, Italy